A lattice modelling framework for fracture-induced acoustic emission wave propagation in concrete

Zhou, Yubao; Aydin, Beyazit Bestami; Zhang, Fengqiao; Hendriks, Max A.N.; Yang, Yuguang

DOI
10.1016/j.engfracmech.2024.110589

Publication date
2024

Document Version
Final published version

Published in
Engineering Fracture Mechanics

Engineering Fracture Mechanics 312 (2024) 110589

Contents lists available at ScienceDirect

Engineering Fracture Mechanics

journal homepage: www.elsevier.com/locate/engfracmech

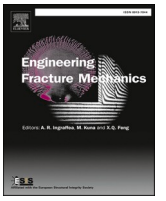

A lattice modelling framework for fracture-induced acoustic emission wave propagation in concrete

Yubao Zhou [a,*], Beyazit Bestami Aydin [a,b], Fengqiao Zhang [a,c], Max A.N. Hendriks [a,d], Yuguang Yang [a]

[a] Faculty of Civil Engineering and Geosciences, Delft University of Technology, 2628CN Delft, the Netherlands
[b] Department of Civil Engineering, Middle East Technical University (METU), 06800 Ankara, Turkey
[c] Department of Engineering, University of Cambridge, CB3 0FA, United Kingdom
[d] Department of Structural Engineering, Norwegian University of Science and Technology, 7491 Trondheim, Norway

ARTICLE INFO

Keywords:
Acoustic emission (AE)
Concrete fracture
Dynamic lattice model
Rayleigh damping
Wave attenuation
Wave propagation
Mesh dependence

ABSTRACT

To date, there is no comprehensive approach available that can explicitly model the complete transient waveforms of acoustic emissions (AE) induced by fracture processes in brittle and quasi-brittle materials like concrete. The complexity of AE modelling arises from the intricate coupling between the local discontinuity of material fracturing and the global continuity of elastic wave propagation in solids. Among others, the lattice type models are promising approaches, as they are known to be a matured modelling approach to simulate the fracturing process in concrete-like materials. Nevertheless, like other discrete element methods (DEM), they are currently limited to describing the number and rate of AE events (broken elements) in the fracture process and cannot explicitly model wave generation and propagation. In this study, we propose a lattice modeling framework to simulate the propagation of complete waveforms of fracture-induced AE signals in concrete. A proportional-integral-derivative (PID) control algorithm is incorporated in an explicit time integration procedure to reduce dynamic noise from spurious oscillations. Additionally, a Rayleigh damping-based calculation method and corresponding calibration procedure are proposed to model the attenuation of AE signals due to material damping. Using the developed approach, we systematically investigate the feasibility of lattice models for elastic wave propagation simulation, the dependence of lattice mesh sizes and the choice of numerical damping parameters. These results lead to a systematic framework which can be employed in simulating wave propagation with attenuation using DEM models in general including lattice models.

1. Introduction

Acoustic emission (AE) monitoring is a promising technique for characterizing the microscopic fracturing phenomena in different brittle and quasi-brittle materials like concrete and for health monitoring of in-service concrete structures. The physical nature of the monitored AE signals lies in the elastic waves induced by local rapid energy release and propagating through the bulk (possibly damaged) concrete of the monitored structures. The sources of AE signals are typically related to local fracturing phenomena, namely

* Corresponding author.
E-mail addresses: y.zhou-16@tudelft.nl (Y. Zhou), b.b.aydin@tudelft.nl (B.B. Aydin), f.zhang-5@tudelft.nl (F. Zhang), M.A.N.Hendriks@tudelft.nl (M.A.N. Hendriks), Yuguang.Yang@tudelft.nl (Y. Yang).

https://doi.org/10.1016/j.engfracmech.2024.110589
Received 13 July 2024; Received in revised form 21 October 2024; Accepted 22 October 2024
Available online 30 October 2024

Nomenclature

AE	acoustic emission
AIC	Akaike information criterion
DEM	discrete element method
DPC	dry-point-contact transducer
FEM	finite element method
A	wave amplitude
$A^{(effective)}$	effective wave amplitude
A^*	lattice element cross-sectional area
a_1	first tensile softening coefficient
a_2	second tensile softening coefficient
a_3	third tensile softening coefficient
$\boldsymbol{C}$	damping matrix
c	damping
c_0	critical damping
d	lattice grid size
E	Young's modulus
e	PID tracking error
$\boldsymbol{F}$	internal nodal force vector
F	nodal force
F_e	element force
f_c	compressive strength
f_{max}	cut-off frequency
f_{Ny}	Nyquist frequency
f_s	sampling frequency
f_t	tensile strength
G_f	fracture energy
$\boldsymbol{K}$	stiffness matrix
k	stiffness of a wave particle
l	lattice element size
$\boldsymbol{M}$	mass matrix
m	mass of a wave particle
n	number of wave cycles
r	distance
Δr	relative distance
S	acoustic emission sensor
T	wave period
t	time
t_{max}	total processing time
Δt	time step
$\boldsymbol{u}$	displacement vector
u	nodal displacement
u_c	actual calculated nodal displacement
$\dot{\boldsymbol{u}}$	velocity vector
$\dot{u}$	nodal velocity
$\ddot{\boldsymbol{u}}$	acceleration vector
$\ddot{u}$	nodal acceleration
V	wave velocity
V_p	pressure wave velocity
V_R	Rayleigh wave velocity
V_s	shear wave velocity
α	mass-proportional damping coefficient
β	stiffness-proportional damping coefficient
β_c	a critical value of β
γ	attenuation from material damping
$\widetilde{\gamma}_k$	normalized attenuation of material damping
$\gamma_{\text{logarithmic}}$	logarithmic decrement
ε	element strain

ε_{cr}	cracking strain
η	material damping factor
η_0	wave geometric spreading loss variable
η_R	material damping of Rayleigh wave
λ_p	pressure wavelength
λ_{p_Ny}	Nyquist pressure wavelength
ξ	damping ratio
ρ	density
υ	dynamic Poisson's ratio
ω	wave angular frequency
φ	wave phase angle

crack nucleation and growth in concrete [1]. As a passive monitoring technique, AE monitoring has distinguished advantages in the prompt detection of early cracking and is suitable for real-time monitoring. However, current applications of AE technique are mostly limited to the AE source localization [2,3] and source classification [4,5] based on phenomenological observations. It remains a challenge to relate the local fracturing phenomena of concrete to the received AE signals after propagation in concrete structures, therefore, resulting in a lack of fundamental understanding and physically based explanation for most parameters of measured AE signals [6,7]. Signals that are received by AE sensors are not only the direct results of vibrations during the fracturing process of concrete, but also the result of the propagation of AE waves and the response of AE sensors. A quantitative relationship between received AE signals and corresponding internal cracking process is not trivial [6,7]. The lack of deterministic models for quantitative AE source characterization leads to inaccurate or even conflicting interpretation for AE measurements [8,9], thus largely restricting reliable AE applications.

In view of the complexity of AE phenomenon, forward modelling is more promising to establish quantitative AE source characterization models than experimental reversal. In numerical modelling, the influence from fracture source, wave propagation and sensor response on AE signals can be separately considered. In this regard, accurately modelling the complete transient waveforms of fracture-induced AE signals is a prerequisite. Nevertheless, there is currently no available approach that can explicitly model the complete transient fracture-induced AE waveforms. The available numerical AE simulation methods are mainly the continuum-based finite element methods (FEM) [10–12] and the discrete element methods (DEM) [13,14]. FEM and DEM face the difficulties in modelling fracture (AE) sources and the propagation of fracture-induced elastic waves, respectively. In typical FEM simulations of a AE process, AE sources are externally introduced by an assumed force/displacement–time function irrelevant to material fracture and without clear physical meanings [15]. DEM simulations are suitable for describing the microscopic fracture behaviors but cannot accurately simulate fracture-induced elastodynamic response of wave propagation and attenuation in solids [16]. Apart from the traditional FEM and DEM models, several other numerical methods have also been employed for AE simulations, such as the elastodynamic finite integration technique [17], combined finite-discrete element method [12] and extended finite element method [18]. Despite these advancements in numerical methods for AE simulations, modelling the complete AE process remains a formidable challenge. This complexity arises from the need to concurrently consider both the local discontinuity of material fracturing (AE source) and the global continuity of wave propagation in solids. Current methods do not adequately address the intricate coupling between these two aspects.

Among others, lattice type models are one of the most promising methods for modelling the complete transient fracture-induced AE waveforms due to the ability to simultaneously describe microscopic discontinuity (for fracture source modelling) and macroscopic continuity (for wave propagation modelling) of solids. In lattice modelling, a continuum is represented by a set of distributed nodes (lumped masses). The bond interactions between lumped masses are explicitly established by lattice elements that can be truss, spring or beam elements [19]. The interaction laws in lattice elements are deduced from classical continuum mechanics and thus the continuity of solids at macroscopic level can be better described than traditional DEM [20]. The irreversible phenomenon of microscopic crack initiation and subsequent growth can be effectively simulated within a lattice framework by incorporating nonlinear constitutive laws allowing the breakage of lattice elements upon reaching critical conditions [21]. Due to these advantages of lattice type models, they have been used to illuminate the damage mechanisms of different quasi-brittle materials in various aspects [22], such as nonlinear repose due to material randomness, brittleness number, fractal dimension and global damage indexes from AE measurements.

Various valuable attempts have been made to explicitly model the complete AE waveforms generated by breaking lattice elements using different versions of lattice models [23–25]. Nevertheless, in listed literature, the simulated AE waveforms are largely different from the experimentally measured AE signals in both time and frequency domains. To achieve full-waveform simulation of fracture-induced AE, it is essential to properly simulate the propagation of elastic waves in lattice modelling. To achieve that, there are several difficulties faced by the lattice modelling approach. First, an accurate time integration technique is needed to ensure the computational accuracy of motion equations in a dynamic lattice model. As shown in the work of Minozzi et al. [25], the computational errors in integration procedure leads to high-amplitude noise signals. Second, although it can better describe the macroscopic continuity of solids than traditional DEM, a lattice model is locally inhomogeneous and, strictly speaking, performs differently than isotropic materials [26]. The influence of such deviation in simulating AE wave propagation with a lattice model has not yet been investigated in literature. Third, it is essential to accurately model the attenuation of elastic wave for properly simulating the complete transient AE waveforms. There is however no systematic approach to accurately consider the attenuation of AE waves using a lattice model.

This paper studies in detail the feasibility and limitation of using lattice modelling to simulate elastic wave propagation in concrete

by considering the above three identified challenges. Based on that, a systematic framework is proposed to accurately simulate the propagation of AE wave signals including wave attenuation by lattice modelling. The proposed approach includes:

- A proportional-integral-derivative (PID) control algorithm to control the dynamic noises other than fracture-induced response (i.e., fracture-induced AE signals) in an explicit time integration procedure.
- A Rayleigh damping-based theoretical method which has been experimentally validated to model the attenuation of AE signals.
- A relationship between lattice grid size and the frequency resolution of simulated AE signals.

By adapting the proposed modelling framework, the propagation with attenuation of elastic waves induced by material fracture can be accurately simulated by DEM models in general including different versions of dynamic lattice models, offering modelling guidelines to achieve full-waveform simulation of AE signals induced in the fracture process of concrete-like materials. The developed modelling approach contributes to a deeper understanding on AE-related fracture mechanisms and thus more reliable and practical applications of AE technique on the monitoring of in-service concrete structures. The findings and proposed methods can be also of interest for other numerical methods, and for other brittle and quasi-brittle materials (e.g., rocks).

This paper focuses on demonstrating the proposed lattice modelling framework in simulating AE wave propagation and attenuation, analyzing only the elastodynamic response induced by a single broken lattice element. Due to space constraints, the simulation of multiple acoustic emission waveforms induced in real concrete progressive fracture process by implementing the proposed lattice modelling approach will be reported in a following-up study. This paper is organized as follows. Section 2 describes the basic concept of lattice modelling and the new techniques implemented in this study. Section 3 verifies the feasibility of proposed method against theoretical solutions for simulating undamped elastic wave propagation using a simple externally inputted wave source function. Section 4 investigates the undamped numerical elastodynamic response of wave propagation induced by the breakage of a lattice element (namely fracture-induced AE signals). Section 5 introduces a systematic test-based calibration procedure for simulating the attenuation of fracture-induced AE signals. Section 6 discusses the choices of representing an AE signal in numerical modelling and the limitations of proposed method.

2. Methodology

This section introduces the proposed lattice modelling framework. Section 2.1 briefly describes the adopted version of lattice model. Section 2.2 and Section 2.3 show two new implemented techniques to incorporate wave propagation and attenuation simulation in lattice modelling, including a proportional-integral-derivative (PID) control algorithm in an explicit time integration scheme for numerical noise reduction and a Rayleigh damping-bases theoretical method for AE wave attenuation simulation.

2.1. Description of adopted lattice model

This study uses a two-dimensional truss-based lattice model. The adopted version of the lattice model was initially developed by Aydin et al. [27], which has been extended in order to simulate the fracturing behavior of plain concrete structures subject to tension [27] and compression [28] and the structural response of different reinforced concrete members [29–31].

In the adopted lattice model, a continuum is represented by a set of uniformly distributed nodes (lumped masses) interconnected by unidimensional truss elements. A two-dimensional squared lattice network is used in this study, corresponding to the classical lattice geometry proposed by Hrennikoff [32]. A basic unit of the adopted lattice network is shown in Fig. 1. The minimum spacing between two neighboring nodes is called grid size, denoted as d. The total mass of an area with the size of $d \times d$ (in 2D case) around a node is lumped into a dimensionless mass at the node. The lumped mass of each node is calculated as $d^2w\rho$, where w and ρ denote the specimen thickness and material density, respectively. The values of lumped masses at boundary and corner nodes are adjusted into $d^2w\rho/2$ and $d^2w\rho/4$, respectively, to match their actual representing areas. Two types of elements are employed at grid level, including the

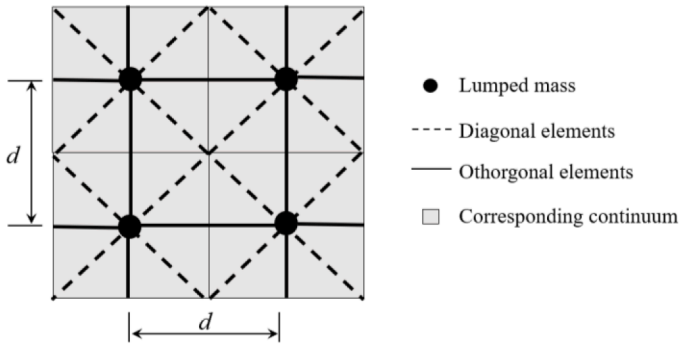

Fig. 1. A basic unit of the two-dimensional truss-based lattice network.

orthogonal elements with size $l = d$ and diagonal elements with size $l = \sqrt{2}d$. It should be mentioned that the lattice models cannot precisely represent a locally isotropic continuum. Unlike an isotropic continuum, the lateral deformation of a lattice network is dependent on the lattice geometry with respect to the loading direction. The inherent Poisson's ratio of the adopted truss-based lattice model varies from 0.26 (in orthogonal directions) to 0.42 (in diagonal directions) depending on the loading direction, resulting an average value at around 0.3 [28]. An introduction on different lattice geometries and resultant Poisson's ratio values of represented continuum is detailed in the work of Rinaldi et al. [26].

The force-strain constitutive law of the truss elements is shown in Fig. 2. The elastic stiffness of truss elements is taken constant as $EA^*(d)$, where E and $A^*(d)$ are concrete modulus of elasticity and effective cross-sectional area of the truss elements, respectively, in which the latter is a function of the lattice grid size d. $A^*(d)$ acts as a bridge linking the elastic properties of discrete lattice elements to those of represented continuum. Specifically, the $EA^*(d)$ value can be viewed as the slope of the linear range of constitutive force-strain diagram (Fig. 2) and is determined by equaling the total elastic energy of a continuum to that of the equivalent lattice model under a uniform strain field. Appendix A provides more details about the relationship between $A^*(d)$ and the elastic properties of represented continuum. The compressive force in the truss elements is assumed to be linear elastic. The tensile force in the truss elements is assumed to be linear until the critical tensile strain ε_{cr} is reached, followed by a tri-linear softening curve. The value of ε_{cr} is taken as a material property and determined as $\varepsilon_{cr} = \frac{f_t}{E}$, where f_t is concrete tensile strength. The tensile softening curve is defined by three parameters, namely a_1, a_2 and a_3, see Fig. 2. They are determined through a calibration procedure with the purpose of matching the lattice simulation with the uniaxial stress–average displacement response of a tension test. A more detailed description for the calibration procedure of the softening parameters can be found in the previous study [28].

Fig. 3 shows the solution flowchart of the adopted lattice model. In each time step, the equations of motion are obtained from equilibrium conditions of all the forces acting on the nodal masses:

$$\boldsymbol{M}\ddot{\boldsymbol{u}}(t) + \boldsymbol{C}\dot{\boldsymbol{u}}(t) + \boldsymbol{F}(t) - \boldsymbol{P}(t) = 0 \tag{1}$$

where $\ddot{\boldsymbol{u}}(t)$ and $\dot{\boldsymbol{u}}(t)$ are the acceleration and velocity vectors, respectively. $\boldsymbol{M}$ and $\boldsymbol{C}$ are the diagonal mass and damping matrices. $\boldsymbol{F}(t)$ and $\boldsymbol{P}(t)$ are the internal and external force vectors. In this study, the damping matrix $\boldsymbol{C}$ is approximated by the Rayleigh damping [33]:

$$\boldsymbol{C} = \alpha\boldsymbol{M} + \beta\boldsymbol{K} \tag{2}$$

where $\boldsymbol{K}$ is the stiffness matrix. α and β are the mass-proportional and stiffness-proportional Rayleigh damping coefficients, respectively. The explicit time integration method proposed by Chung & Lee [34] is adopted to solve the equations of motion. A more detailed description of the solutions strategy adapted by the lattice model is discussed in previous works of the authors [27,30].

2.2. PID control for noise signal reduction

In the lattice modeling approach, the fracture-induced AE signals are assumed to be the elastodynamic response of concrete induced by breakage of elements locally. This effect can be simulated directly in lattice models by solving the motion equations (Eq. (1)) using an explicit time integration scheme. This scheme, however, also introduces dynamic noises, called spurious oscillations [35]. The spurious oscillations are largely amplified in case of unstable external loading [36]. In a direct solver, external loading bias is inevitable, and it amplifies the spurious oscillations into high-amplitude dynamic noise in the system (see also Section 4.1). This can be suppressed by controlling the external loading bias. In this paper, we propose to minimize noise signals caused by external loading bias by implementing a proportional-integral-derivative (PID) control scheme in the lattice model. The PID algorithm serves as a feedback loop controller and can be mathematically describe as follows:

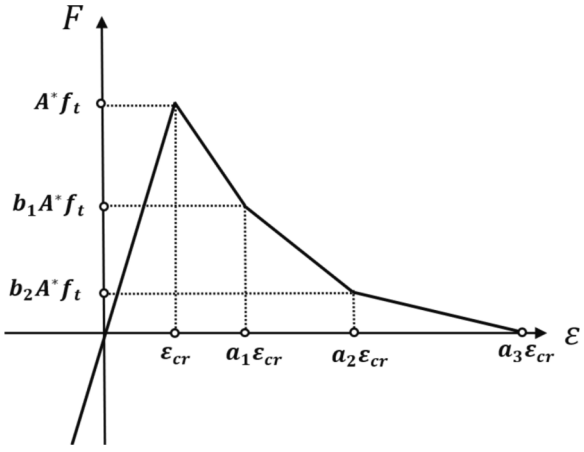

Fig. 2. Adopted force-strain constitutive law for the truss elements ($b_1 = 0.6$ and $b_2 = 0.2$) [27].

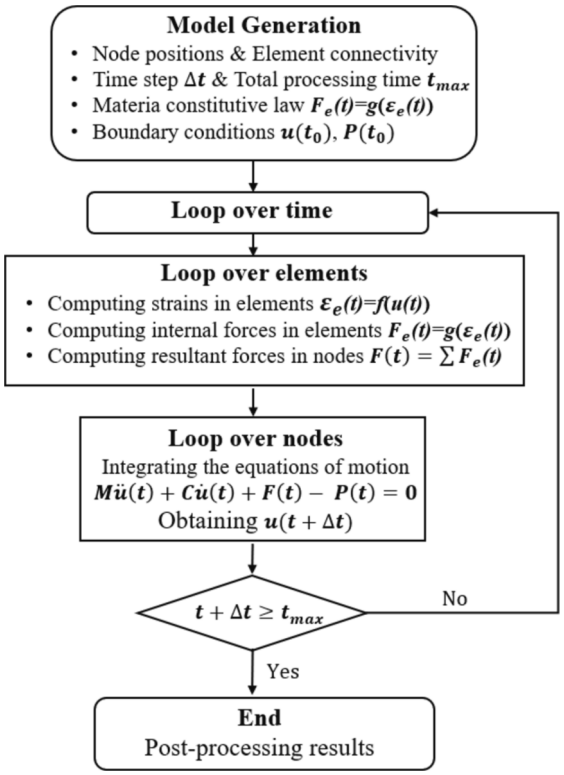

Fig. 3. Solution flowchart of the adopted lattice model [27].

$$\dot{P}(t) = K_p e(t) + K_i \int_0^t e(t)dt + K_d \frac{de}{dt} \tag{3}$$

where $\dot{P}(t)$ and $e(t)$ are the external loading rate and tracking error, respectively. K_p, K_i and K_d are three coefficients controlling the proportional gain, integral gain and derivative gain of $e(t)$, respectively. Consider an arbitrary system (Fig. 4), the loading rate function $\dot{P}(t)$ can be controlled in multiple ways by controlling the displacement rate at Point A, relative displacement rate between Points A and B, crack width opening rate at Point C, or stress/strain rate at Point D. Assuming that the targeted control variable is the displacement of loading point $u(t)$ and the actual calculated displacement is $u_c(t)$, the tracking error is calculated as $e(t) = u(t) - u_c(t)$. The rate of external load $\dot{P}(t)$ defined by the integro-differential equation (Eq. (3)) is solved to update the value of $P(t)$ as feedback in each calculation step (Eq. (1)). The bias in nodal velocity or acceleration induced by external loading $P(t)$ (i.e., noise signals) can be sufficiently reduced by keeping the values of error function at a low level. Values of PID constants used in this study are chosen according to the recommendation from Ziegler and Nichols [37]. Integrating PID control within the explicit time integration methodology avoid additional dynamic effects from external loading bias. Effect of the implemented PID control will be demonstrated in Section 4.1.

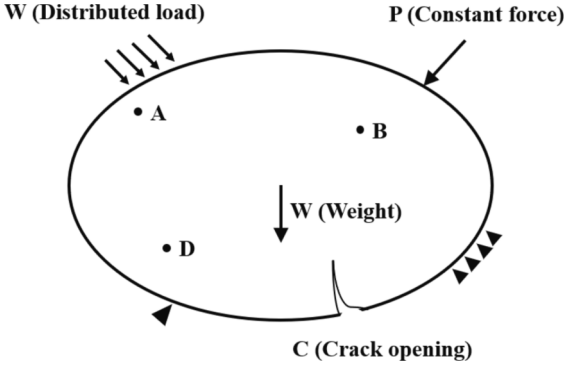

Fig. 4. An arbitrary system with PID control.

2.3. A Rayleigh damping based method for AE signal attenuation

To properly simulate the propagation of elastic waves in concrete, it is essential that the modelling approach can consider the attenuation of AE signals. The attenuation of AE signals (elastic waves) in concrete is caused by many factors [38]. Among others, two main factors can be distinguished, namely, geometric spreading loss (or called geometric attenuation) and material damping [39]. The geometric spreading loss is the loss of wave amplitude due to the radiation of a wave front departing from a point source into all directions [38]. The material damping (also referred to as viscous damping [40] or absorbing damping [41]) describes the energy stored in a wave that is dissipated due to viscoelastic material behavior, which further includes the intrinsic damping and scattering damping [39]. The intrinsic damping is associated with the internal friction between particles [42], while the scattering damping is associated with the fact that wave with certain wavelength scatters in the media when it travels through scatters of comparable sizes (e.g., aggregates or pores in concrete) [43].

The wave attenuation due to spreading loss has been inherently considered in the adopted lattice model (this will be demonstrated in Section 3.2), as the system energy conservation is accurately considered in the establishment of force equilibrium (Eq. (1)). A Rayleigh damping-based method is proposed in this paper to consider the wave attenuation due to material damping. Derivation of the proposed method is described in the following.

As the intrinsic damping and scattering damping are hard to be distinguished from each other, they are often described together by a frequency-dependent material damping factor [44], herein denoted as $\eta(\omega)$. $\eta(\omega)$ depends on the frequency and the type of a wave: a wave of higher frequency attenuates faster because the wave involves more cycles of particle movements during the same travel time [45]; shear and Rayleigh waves attenuate more than pressure wave owing to more friction between motion particles in shear deformation [46]. For a single-frequency and single-mode wave with angular frequency ω, the ratio between two wave peak amplitudes, $A_i(\omega)$ and $A_j(\omega)$, received at two different locations i and j, respectively, with distances of r_i and r_j to the wave source is described as [40]:

$$\frac{A_i(\omega)}{A_j(\omega)} = \left(\frac{r_j}{r_i}\right)^{\eta_0} \exp[-\eta(\omega)(r_i - r_j)] \tag{4}$$

where $\left(\frac{r_j}{r_i}\right)^{\eta_0}$ is the wave attenuation considering geometric spreading loss and η_0 is a controlling variable with $\eta_0 = 0$ for plane wavefront, $\eta_0 = 0.5$ for cylindrical and circular wavefronts and $\eta_0 = 1.0$ for spherical wavefronts propagating in isotropic and homogeneous media [40]. $\mathrm{Exp}[-\eta(\omega)(r_i - r_j)]$ represents the wave attenuation due to material damping. Based on Eq. (4), the frequency-dependent material damping factor $\eta(\omega)$ can be expressed as:

$$\eta(\omega) = \frac{1}{r_i - r_j}\left(\ln\frac{A_j(\omega)}{A_i(\omega)} - \eta_0 ln\frac{r_i}{r_j}\right) \tag{5}$$

According to Eq. (5), the attenuation of wave amplitudes excluding the geometric spreading loss between locations i and j, denoted as $\gamma(\omega)$, can be expressed as:

$$\gamma(\omega) = \ln\frac{A_j(\omega)}{A_i(\omega)} - \eta_0 ln\frac{r_i}{r_j} = (r_i - r_j)\eta(\omega) = \Delta r\eta(\omega) \tag{6}$$

where $\Delta r = r_i - r_j$ is the distance between two receiving locations i and j. If $V(\omega)$ is the velocity of the considered single-mode wave, the arrival time difference of waves received at locations i and j, denoted as $\Delta t = t_i - t_j$, can be expressed as:

$$\Delta t = t_i - t_j = \frac{r_i - r_j}{V(\omega)} = \frac{\Delta r}{V(\omega)} \tag{7}$$

Assuming the two locations i and j are chosen in such a way that Δt can be expressed as the product of the number of wave cycles n and the wave period $T = \frac{2\pi}{\omega}$, Eq. (7) can be further expressed as [38]:

$$\Delta t = \frac{\Delta r}{V(\omega)} = nT = \frac{2\pi n}{\omega} \tag{8}$$

By substituting Eq. (8) into Eq. (6), $\gamma(\omega)$ is then expressed as:

$$\gamma(\omega) = \frac{2\pi n}{\omega} V(\omega)\eta(\omega) \tag{9}$$

Alternatively, consider the motion of a wave particle involved in the single-frequency and single-mode wave. The vibration amplitude of the wave particles attenuates in the time domain following a logarithmic decrement law. The logarithmic decrement, denoted as $\gamma_{\mathrm{logarithmic}}(\omega)$, is given by the following equation [47]:

$$\gamma_{\mathrm{logarithmic}}(\omega) = ln\frac{A_1}{A_n} = \frac{2n\pi\xi(\omega)}{\sqrt{1 - \xi(\omega)^2}} \tag{10}$$

where A_1 and A_n are the vibration amplitudes of the wave particle at first cycle and after n cycles, respectively. $\xi(\omega)$ is damping ratio. In a low-damping system, $\xi(\omega) \ll 1$, Eq. (10) can be approximated to:

$$\gamma_{\text{logarithmic}}(\omega) = ln\frac{A_1}{A_n} \approx 2n\pi\xi(\omega) \tag{11}$$

The damping ratio $\xi(\omega)$ can be expressed in the form of Rayleigh damping $c = \alpha m + \beta k$ as proposed by Caughey [33]:

$$\xi(\omega) = \frac{c}{c_0} = \frac{\alpha m + \beta k}{2\sqrt{km}} = \frac{1}{2}\left(\alpha\sqrt{\frac{m}{k}} + \beta\sqrt{\frac{k}{m}}\right) = \frac{1}{2}\left(\frac{\alpha}{\omega} + \beta\omega\right) \tag{12}$$

where m, k and $\omega = \sqrt{\frac{k}{m}}$ are mass, stiffness and natural angular frequency of the wave particle. $c_0 = 2\sqrt{km}$ is the critical damping. Furthermore, it is assumed that in the case of a single-frequency and single-mode wave propagating in isotropic and homogeneous media, the attenuation of the motion of an involved wave particle in time domain, $\gamma_{\text{logarithmic}}(\omega)$, is equivalent to the spatial attenuation of the wave excluding geometric spreading loss, $\gamma(\omega)$, both caused by the material damping which is dependent on the wave frequency [38,41,48]. Accordingly, Eq. (9) is equal to Eq. (11), as follows:

$$\gamma(\omega) = \frac{2\pi n}{\omega} V(\omega)\eta(\omega) = \gamma_{\text{logarithmic}}(\omega) = 2n\pi\xi(\omega) \tag{13}$$

By substituting Eq. (12) into Eq. (13), the relationship between the material damping factor $\eta(\omega)$ and Rayleigh damping coefficients α and β is established as:

$$\eta(\omega) = \frac{2\pi f\xi(\omega)}{V(\omega)} = \frac{\omega}{2V(\omega)}\left(\frac{\alpha}{\omega} + \beta\omega\right) = \frac{1}{2V(\omega)}\left(\alpha + \beta\omega^2\right) \tag{14}$$

Eq. (14) is derived based on the assumption of a single-mode wave. We assume that the attenuation an AE signal attenuates in the same way. The damping factor of an AE signal in an interested frequency range (ω_1, ω_2) can then be described by one set of suitable Rayleigh damping coefficients using Eq. (14). Specifically, by substituting the low- and high-bound frequency ω_1 and ω_2, corresponding material damping factors $\eta(\omega_1)$ and $\eta(\omega_2)$, and wave velocities $V(\omega_1)$ and $V(\omega_2)$ of a dominating wave mode into Eq. (14), we get the following equation set:

$$\begin{cases} \eta(\omega_1) = \dfrac{1}{2V(\omega_1)}\left(\alpha + \beta{\omega_1}^2\right) \\ \eta(\omega_2) = \dfrac{1}{2V(\omega_2)}\left(\alpha + \beta{\omega_2}^2\right) \end{cases} \tag{15}$$

By solving Eq. (15), average Rayleigh damping coefficients covering an interested frequency range (ω_1, ω_2) of an AE signal with certain dominating wave mode, denoted as $\alpha(\omega_1, \omega_2)$ and $\beta(\omega_1, \omega_2)$, can be determined as:

$$\alpha(\omega_1, \omega_2) = \frac{2[V(\omega_2)\eta(\omega_2){\omega_1}^2 - V(\omega_1)\eta(\omega_1){\omega_2}^2]}{{\omega_1}^2 - {\omega_2}^2} \tag{16}$$

$$\beta(\omega_1, \omega_2) = \frac{2[V(\omega_1)\eta(\omega_1) - V(\omega_2)\eta(\omega_2)]}{{\omega_1}^2 - {\omega_2}^2} \tag{17}$$

3. Verification of undamped elastic wave propagation in lattice model

In this section, the proposed lattice model is verified using four simplified cases of two different signal source forms, namely, plane waves and point-source waves. In the verification cases, the models assume undamped elastic wave propagation, so that one may

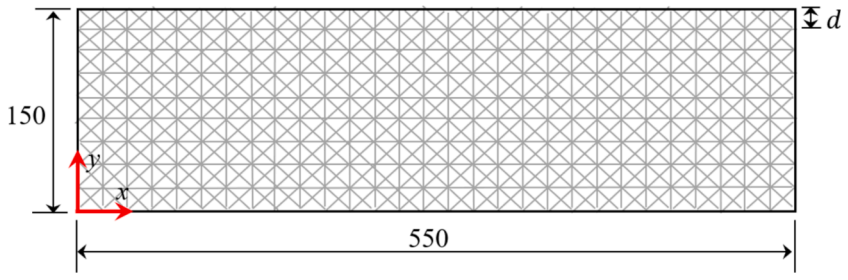

Fig. 5. Numerical model for the simulations of undamped elastic wave propagation (unit: mm).

compare the simulated results with classical theoretical solutions. A concrete beam specimen with dimensions of 550 × 150 × 40 (length × width × thickness) mm^3 is modelled with 1-mm lattice grid size (d = 1mm). For a clear discussion, a Cartesian frame is defined with the coordinate origin located at the bottom left corner of the numerical model, see Fig. 5. The adopted material properties are listed in Table 1.

A nodal displacement $u_i(t)$ is defined as the wave source function at the corresponding source location. The adopted wave source function $u_i(t)$ was initially proposed in Bruna & Riera [49] as a typical numerical representation of hypocenters:

$$u_i(t) = u_0 \sin(\omega_0)\sin(\pi\frac{t-t_a}{t_a-t_b}), t_a < t < t_b \tag{18}$$

where the subscript $i = x, y$ of $u_i(t)$ denotes the nodal displacement directions in x or y directions. $u_0 = 2.5 \times 10^{-6}$ mm, $t_a = 0$, $t_b =$ 0.01ms and $\omega_0 = 2\pi \times 200$kHz. These parameters result in a Gaussian pulse with a central frequency 200kHz and a duration of 0.01ms.

A time step of 2×10^{-4}ms (5 MHz sampling rate) and zero numerical damping ($\alpha = \beta = 0$) are used in the explicit integration procedure when solved the model.

3.1. Plane waves

The propagation of the plane pressure (P) and shear (S) waves is examined in this sub-section through two simulation cases. The plane waves are considered propagating from left (x = 0mm) to right plane (x = 550mm) in x direction. The applied boundary conditions are summarized in Table 2, where Case 1 and Case 2 correspond to the simulation of P wave and S wave, respectively. The source displacements $u_i(t)$ are applied to all the nodes at plane x = 0mm in the x and y directions for P wave and S wave, respectively. The symmetric or antisymmetric boundary conditions are introduced at planes y = 0mm and y = 150mm to simulate an infinite space in y direction that allows the unrestricted propagation of plane waves without altering the waveforms [50]. In addition, a nonreflexive boundary is implemented on the right edge to avoid wave reflection. Various methods can be used to create such a nonreflexive boundary, as discussed in [51]. Herein, a simple method was implemented by providing nodes from x = 540mm to x = 550mm with smoothly increased viscous dampers, with their stiffness proportional damping coefficients β linearly increasing from 0 (nodes at x = 540mm) to a critical value β_c (nodes at x = 550mm). β_c is determined by the central angular frequency ω_0 of simulated source wave as [52]:

$$\beta_c = \frac{2}{\omega_0} \tag{19}$$

For Case 1, a typical x direction displacement field at simulation time t = 0.1ms is illustrated in Fig. 6a. Fig. 6b shows the evolution of displacements in x direction of the two recorded nodes at (x = 0,y = 75mm) and (x = 100mm,y = 75mm). The P-wave velocity in the lattice model can be estimated using the distance and arrival time difference of two recorded nodes. The arrival time of P-wave at x = 100mm is 22.7 μs and accordingly the numerical P-wave velocity is estimated as $V_{p(numerical)} = \frac{100\text{mm}}{22.7\mu\text{s}} = 4405$m/s.

For Case 2, a typical y direction displacement field at simulation time t = 0.1ms is illustrated in Fig. 7a. Fig. 7b shows the evolution of displacements in y direction of the two recorded nodes at (x = 0,y = 75mm) and (x = 100mm,y = 75mm). The arrival time of S-wave at x = 100mm is 41.8 μs and accordingly the numerical S-wave velocity is estimated as $V_{s(numerical)} = \frac{100\text{mm}}{41.8\mu\text{s}} = 2395$m/s.

For isotropic and homogeneous solids, the theoretical P- and S-wave velocities are calculated by [53]:

$$V_{p(theoretical)} = \sqrt{\frac{(1-\upsilon)E}{(1+\upsilon)(1-2\upsilon)\rho}} \tag{20}$$

$$V_{s(theoretical)} = \sqrt{\frac{E}{2(1+\upsilon)\rho}} \tag{21}$$

Using the material properties listed in Table 1, the theoretical P- and S-wave velocities are calculated as 4238 and 2479 m/s, respectively. The differences between theoretical and numerical wave velocities are 4.2 % and 3.4 % for P- and S-waves, respectively.

3.2. Point-source waves

As the sources of acoustic emission signals can be regarded as point excitations considering the much smaller fracture scale than that of concrete structures, two additional simulation cases are conducted to investigate the propagation of body wave and Rayleigh

Table 1
Concrete material properties.

Properties (unit)	Density ρ (kg/m^3)	Elastic modulus E (GPa)	Compressive strength f_c (MPa)	Tensile strength f_t (MPa)	Fracture energy G_f (N/m)	Dynamic Poisson's ratio υ (−)
Values	2310	35.20	33.95	3.15	58.82	0.24

Table 2
Boundary conditions used for plane wave simulation.

Case number	Wave type	Plane at $x = 0$	Planes at $y = 0, y = 150$mm	Planes at $x = 540 \sim 550$mm	Plane at $x = 550$mm
1	Pressure wave	$u_x(t)$	Symmetry plane	Nonreflexive boundary	$u_x = 0$
2	Shear wave	$u_y(t)$	Anti-symmetry plane	Nonreflexive boundary	$u_x = u_y = 0$

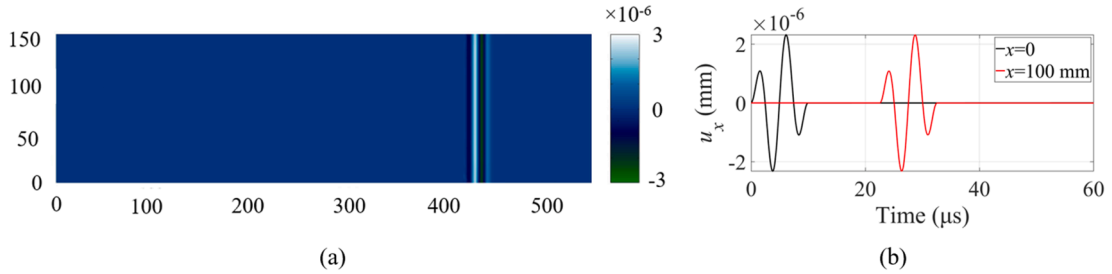

Fig. 6. Simulation results for plane P-wave: (a) a typical x direction displacement filed at simulation time $t = 0.1$ms (unit: mm); (b) evolution of x direction displacements of two recorded nodes at ($x = 0$, y $= 75$mm) and ($x = 100$mm, $y = 75$mm).

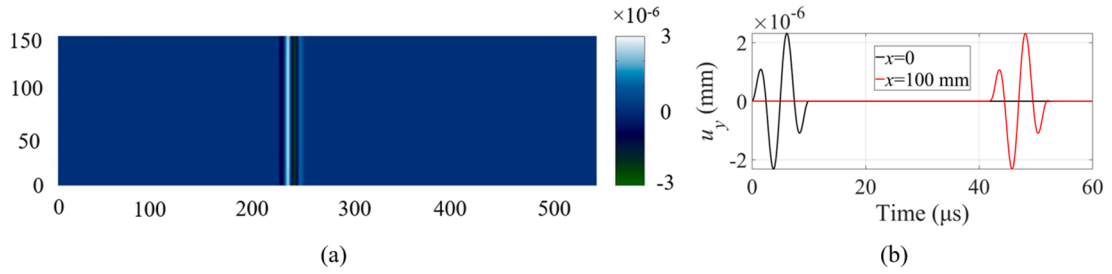

Fig. 7. Simulation results for plane S-wave: (a) a typical y-direction displacement filed at simulation time $t = 0.1$ms (unit: mm); (b) evolution of y-direction displacements of two recorded nodes at ($x = 0, y = 75$mm) and ($x = 100$mm, $y = 75$mm).

wave (R-wave) induced by a point source. The applied boundary conditions are summarized in Table 3. A source displacement $u_y(t)$ (Eq. (17)) is applied in y direction on a single node at ($x = 275$mm, $y = 75$mm) and at ($x = 275$mm, $y = 150$mm), respectively. Case 3 simulates the propagation of a point-source body wave while Case 4 simulates a point source R-wave. The boundary conditions defined at the four edges of both models are given in Table 3.

For Case 3, a typical y direction displacement field at simulation time $t = 0.02$ms is illustrated in Fig. 8a. Due to the directivity of the applied wave source (applied in y direction), the intensity of the wave front is biased in different propagation directions. The P- and S-waves are dominant in y and x directions, respectively. Fig. 8b shows the evolution of displacements in y direction of two recorded nodes at ($x = 275$mm,$y = 75$mm) and ($x = 375$mm,$y = 75$mm). It can be seen that the amplitudes of point-source wave decrease with increasing the wave travel distance due to geometric spreading loss (or wave radiation) [38]. Moreover, the waveform is slightly altered due to the directional dependency of Poisson's ratio in the lattice model. A more detailed discussion about the influence of material anisotropy on the waveform alternation can be found in the study of Iturrioz and Riera [50].

For Case 4, a typical y direction displacement field at simulation time $t = 0.04$ms is illustrated in Fig. 9a. P-, S- and R-waves coexist in this case with the intensity of R-wave being dominant. Fig. 9b shows the evolution of displacements in y direction of two recorded nodes at ($x = 275$mm, $y = 150$mm) and ($x = 375$mm, $y = 150$mm). The attenuation of the undamped R-waves is modelled by

Table 3
Boundary conditions used for point-source wave simulation.

Case number	Wave type	Node at ($x = 275$mm, $y = 75$mm)	Node at ($x = 275$mm, $y = 150$mm)	Planes at $x = 0 \sim 10$mm, $x = 540 \sim 550$mm, $y = 0 \sim 10$mm	Planes at $y = 140 \sim 150$mm	Plane at $y = 0$
3	Body wave	$u_y(t)$	–	Nonreflexive boundary	Nonreflexive boundary	$u_y = 0$
4	Rayleigh wave	–	$u_y(t)$	Nonreflexive boundary	–	$u_y = 0$

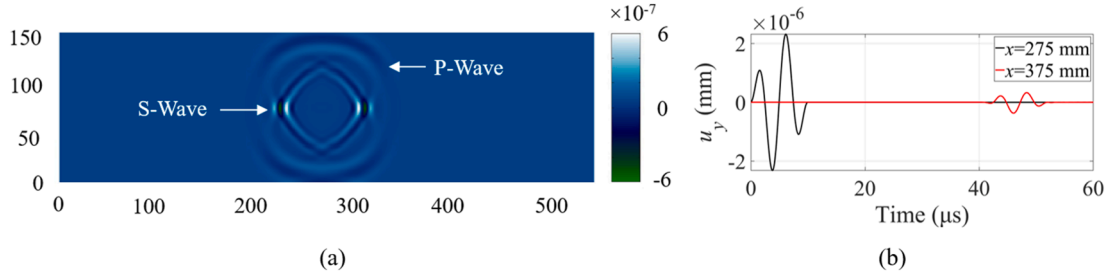

Fig. 8. Simulation results for point-source body wave: (a) a typical y direction displacement filed at simulation time $t = 0.02$ms (unit: mm); (b) evolution of y direction displacements of two recorded nodes at ($x = 275$mm, $y = 75$mm) and ($x = 375$mm, $y = 75$mm).

substituting $\eta_0 = 0.5$ and $\eta(\omega) = 0$ into Eq. (4), the ratio between two peak amplitudes, $A_i(\omega)$ and $A_j(\omega)$, obtained at locations i and j with distances of r_i and r_j from the source is described as:

$$\frac{A_i(\omega)}{A_j(\omega)} = \sqrt{\frac{r_j}{r_i}} \tag{22}$$

Fig. 9c shows the numerical results in comparison with the prediction given by Eq. (22), where the peak amplitudes are normalized with respect to that of a reference node at ($x = 300$mm, $y = 150$mm). It can be found that the numerical results fit well the theoretical curve given by Eq. (22).

Despite the consistency with the theoretical solutions in terms of peak amplitude, similar to Case 3, due to the variation of Poisson's ratio values in the adopted two-dimensional lattice model, the simulated wave velocities are slightly different in different propagation directions. As can be observed in Fig. 8a and Fig. 9a, the simulated wave fronts are distorted circles, especially for the S-waves.

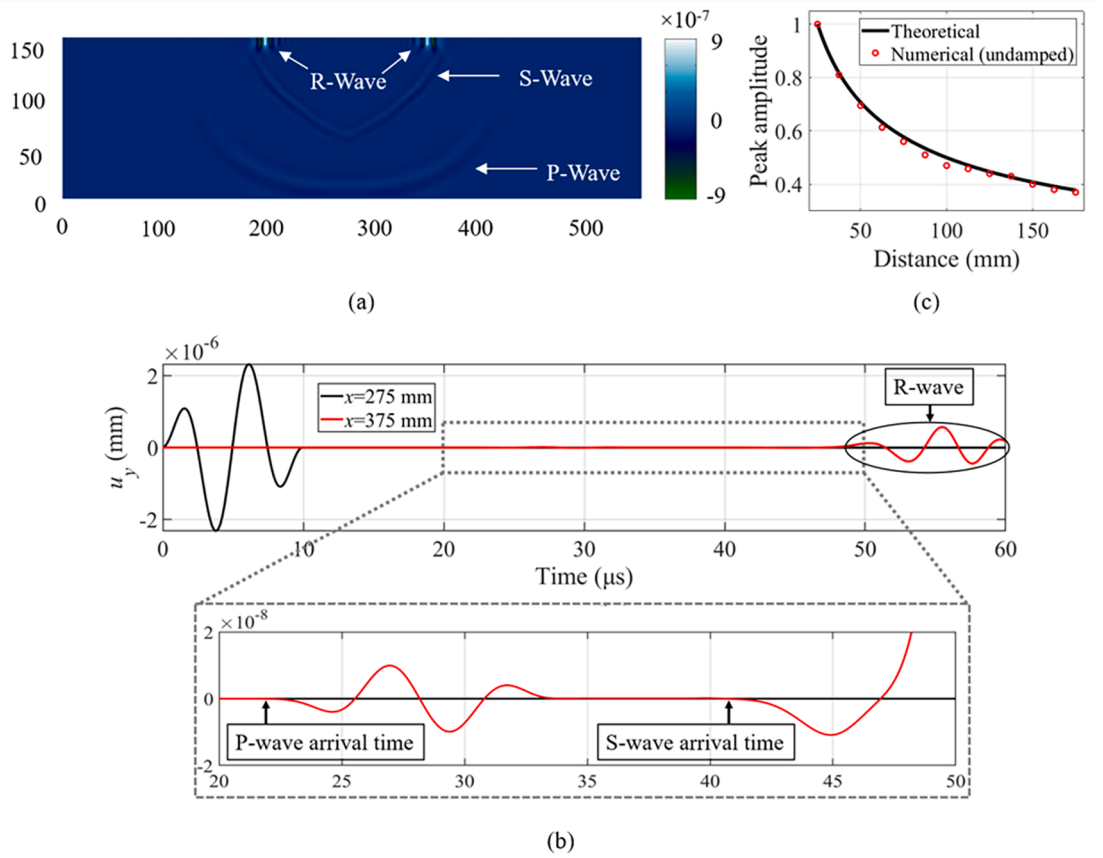

Fig. 9. Simulation results for point-source Rayleigh wave: (a) a typical y direction displacement filed at simulation time $t = 0.04$ms (unit: mm); (b) evolution of y direction displacements of two recorded nodes at ($x = 275$mm, $y = 150$mm) and ($x = 375$mm, $y = 150$mm); (c) a comparison of geometric spreading loss of Rayleigh waves between theoretical calculations and numerical results with zero damping ($\alpha = \beta = 0$).

4. Influence factors on simulating undamped fracture-induced AE signals

This section considers the propagation of undamped AE waves generated by the breakage of a lattice element. The effect of the implemented PID control algorithm and the influence of lattice grid sizes on the simulated undamped AE waveforms are investigated. Limited by the size of this paper, a detailed analysis on the relationship between the breakage of a lattice element and the fracturing process of concrete cannot be discussed in detail. Readers are referred to our previous study [27].

The studied numerical model and its boundary conditions are given in Fig. 10 and is named as simulation Case 5. An additional 1-mm vertical element is placed at location ($x = 50$mm, $y = 150$mm) as the fracture source ($l_{(source)} = 1$mm). The material properties listed in Table 1 are adopted as inputs for the numerical model. Three tensile softening parameters a_1, a_2 and a_3 (Fig. 2) are calibrated as 5.5, 120 and 620. A positive y direction displacement $u_y(t)$ in terms of a constant velocity of 1×10^{-3} mm/s ($\frac{du_y(t)}{dt} = 1 \times 10^{-3}$mm/s) is applied at the upper node of the fracture source element to induce tensile fracturing of the element. Tensile cracking at fracturing process zone (crack tip) and friction along existing cracking surfaces are two main AE sources involved in the fracturing processes of concrete-like quasi-brittle materials [4]. Only the tensile fracture-induced AE signals is considered herein, as this paper focuses on demonstrating wave propagation simulations of the proposed modelling framework. The modelling of AE signals of various source types generated in concrete fracturing processes will be reported in a following-up study.

The PID control algorithm is implemented in the simulations. The controlling variable is the velocity of the loading node (upper node of the fracture source element) to minimize the loading bias. The node located at ($x = 130$mm, $y = 150$mm) is considered as a virtual AE sensor (marked as S1 in Fig. 10). The other virtual sensors marked in Fig. 10 (S2-S6) will be used in the simulation cases in later sections. The vertical (y direction) accelerations recorded at S1 are used to mimic the received AE signals, as received AE signals in reality are the stress waves perpendicular to AE sensor surface [54]. A more detailed discussion about the numerical representation of AE signals is given in Section 6.1. The adopted time step and numerical damping coefficients are 5×10^{-5}ms (20 MHz sampling rate) and zero ($\alpha = \beta = 0$), respectively.

4.1. Effect of implemented PID control algorithm

Two simulation cases with and without the PID control are performed to illustrate the effect of the implemented PID algorithm. The grid size is selected as 1mm ($d = 1$mm in Fig. 10). The evolution of vertical accelerations of virtual AE sensor S1 in the two simulation cases are shown in Fig. 11, where the presented period is from the beginning of the loading process to a moment before fracturing of the source element. It can be found that by introducing the PID algorithm a stable loading process is observed and the dynamic noise in nodal accelerations is effectively suppressed (Fig. 11b) comparing to the simulation case without PID control in which the nodal accelerations have a bias induced by the external loading, with non-vanishing noise signals of high amplitudes existing even in the absence of a lattice element fracture (Fig. 11a). Similar phenomenon was also reported in the work of Minozzi et al. [25], where a 2D lattice model without PID control was used to simulate the dynamic fracture of quasi-brittle materials. The dynamic noises influence the computational accuracy of targeted dynamic response due to a fracturing lattice element; it also leads to the difficulty in identifying the fracture-induced AE signals with relatively low amplitudes, which is mixed by the non-vanishing noises.

4.2. Lattice model grid size & AE signal frequency resolution

As a discrete modelling approach, the grid size has a clear influence of the propagation of AE signals. To demonstrate this, several simulations are performed with varied grid sizes ($d = 1$ 10mm). The AE signal source is controlled by keeping the size of the fracture source element constant ($l_{(source)} = 1$mm). Fig. 12 shows typical simulated AE signals from models with grid sizes of 1 and 2.5 mm. The starting time zero of AE signal presented in Fig. 12 is not the actual simulation time but has been normalized to represent a typical pre-trigger time of 256 us [1]. It can be observed that, the obtained AE signals are largely influenced by the grid sizes. In models with

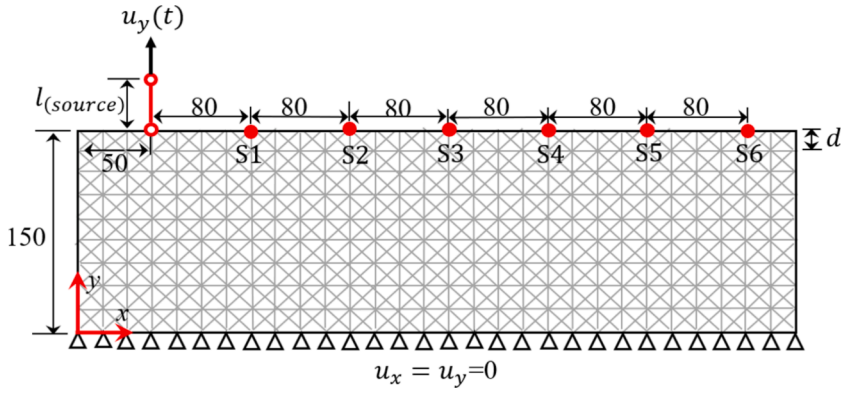

Fig. 10. Numerical model and boundary conditions in Case 5 for simulating the AE signals induced by a fractured lattice element (unit: mm).

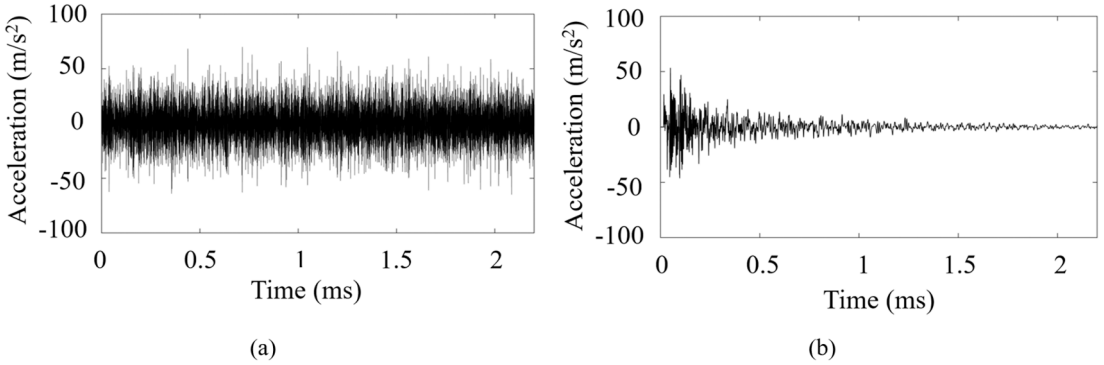

Fig. 11. Vertical accelerations of the virtual AE sensor S1 before fracture occurring for two simulation cases: (a) without PID control and (b) with PID control.

smaller grid sizes higher frequency components of an AE signal are observed. A theoretical explanation of this observation is given below.

The highest frequency that a lattice model with a given grid size can simulate is herein defined as the cut-off frequency, denoted as f_{max}. The corresponding minimum P- wavelength is then denoted as $\lambda_{p(min)}$. In Fig. 12, it should be noted that the signal amplitudes corresponding to frequencies higher than around half of the cut-off frequencies f_{max} are sharply decreased. According to the Nyquist criteria [55], the frequency components higher than half of the maximum frequency that can be produced by a given temporal or spatial sampling rate will lose their information. This phenomenon is called the aliasing [56]. The highest frequency without signal aliasing, herein called Nyquist frequency and denoted as f_{Ny}, is equal to half of the cut-off frequency f_{max}:

$$f_{Ny} = 0.5 f_{max} \tag{23}$$

The minimum P- wavelength without signal aliasing, herein called Nyquist pressure wavelength and is denoted as λ_{p_Ny}, is then calculated by:

$$\lambda_{p\_Ny} = \frac{V_p}{f_{Ny}} = \frac{V_p}{0.5 f_{max}} = 2\lambda_{p(min)} \tag{24}$$

Physically, the adopted truss elements have constant axial deformations (without bending moment), resulting in linear variation of displacement only at their nodes. Therefore, as shown in Fig. 13a, at least four element (5 nodes) are needed to approximate (or spatially sample) a minimum pressure sine wave with wavelength $\lambda_{p(min)}$. Accordingly, as shown in Fig. 13b, at least eight element (9 nodes) are needed to approximate the Nyquist pressure wavelength λ_{p_Ny}:

$$\lambda_{p\_Ny} = 2\lambda_{p(min)} = 8d \tag{25}$$

By substituting Eq. (24) into Eq. (25), a relationship between the Nyquist frequency f_{Ny} and lattice grid size d can be established as:

$$f_{Ny} = \frac{V_p}{8d} \tag{26}$$

The relationship between the lattice grid sizes d and the Nyquist frequency f_{Ny} obtained from both Eq. (26) and from lattice simulations are compared in Fig. 14. The value of f_{Ny} is calculated as half of f_{max} (Eq. (23)). The values of f_{max} from the lattice simulations are

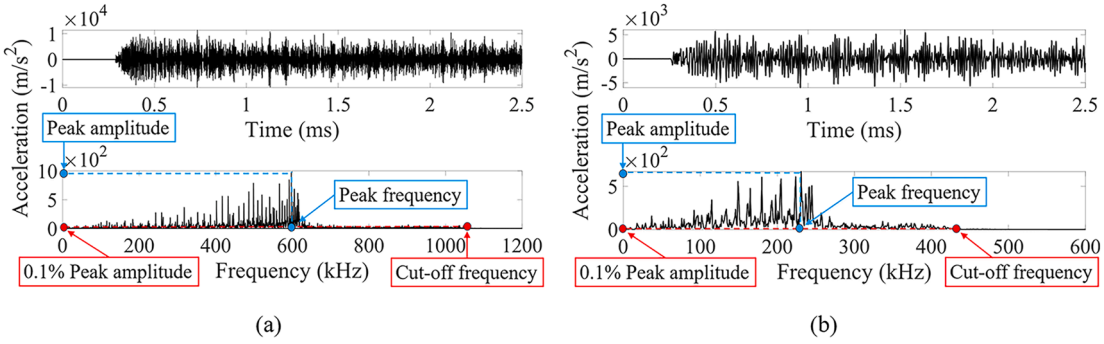

Fig. 12. Simulated AE signals received at virtual sensor S1 for simulation cases with: (a) 1-mm and (b) 2.5-mm grid sizes d and a fixed 1-mm fracture source element size $l_{(source)}$.

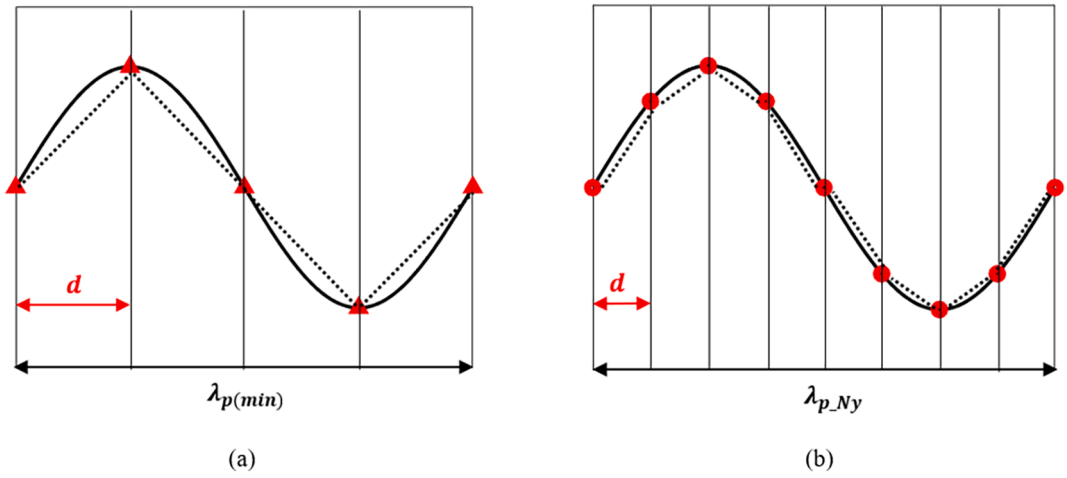

Fig. 13. Physical interpretation for the relationships between: (a) lattice grid size d and the minimum pressure wavelength $\lambda_{p(min)}$ and (b) lattice grid size d and the Nyquist pressure wavelength λ_{p_Ny}.

selected as the frequency in the upper frequency range with an amplitude equal to 0.1 % of the peak amplitude, as shown in Fig. 12. It can be found that the proposed function fits well the simulation data. The requirement defined by Eq. (26) can be a recommendation of lattice grid size: an appropriate lattice grid size d should be selected according to the maximum targeted maximum AE signal frequency, denoted as $f_{\max\_targeted}$, or the minimum targeted pressure wave length, denoted as $\lambda_{p(min\_targeted)}$, as follows:

$$d \le \frac{V_p}{8 f_{\max\_targeted}} \text{ or } d \le \frac{\lambda_{p(min\_targeted)}}{8} \tag{27}$$

5. Rayleigh damping calibration procedure for attenuation of fracture-induced AE signals

This section is dedicated to introducing a systematic test-based calibration procedure for incorporating numerical damping in the lattice modelling approach. The Rayleigh damping calculation method proposed in Section 2.3 is demonstrated through an experiment. The Rayleigh damping coefficients α and β are determined by the experimentally obtained material damping factor $\eta(\omega)$ and the wave velocity $V(\omega)$ (Eq. (16)–(17)). Experimental procedure for evaluating these two parameters is described in the following.

The measurement setup and the calibration specimen are given in Fig. 15. The specimen has the same dimensions of the numerical model discussed in the previous sections (Fig. 10), namely 550 × 150 × 40 mm^3. Different from the simplified model, a notch of 5-mm width and 30-mm depth is present at mid-length of the specimen. A three-point bending test will be applied on the specimen and the results of the test will be reported in a separate paper. The material properties of the specimen are the same with those used in the simulations (Table 1). The concrete has a maximum aggregate size of 8 mm and a designed strength class of C35. The key material parameters of the specimen such as compressive strength f_c, mass density ρ, modulus of elasticity E were obtained by dedicated tests on concrete cubes. The tensile strength f_t and tensile fracture energy G_f are calculated based on the measured value of compressive strength f_c according to fib Model Code 2010 (MC2010) [57]. The dynamic Poisson's ratio value of 0.24 is selected based the measurement for C35-class concrete [58].

The measurement setup consists of a transducer (marked as T0) as signal source and six R15α AE sensors with operating frequency range of 50–400 kHz [59] (marked as S1-S6) as receivers. The signal source T0 is placed at the location (x = 50 mm, y = 150mm) and connected to a Pundit-200 wave generator [60]. Two types of transducers with different wavebands are used to generate source signals

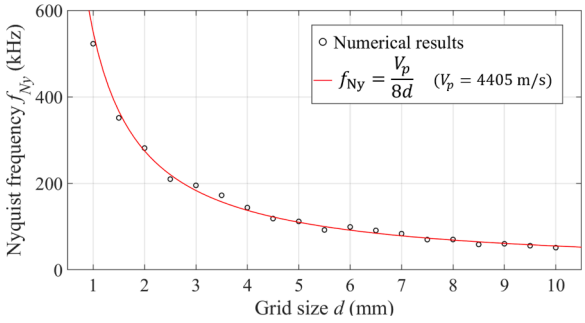

Fig. 14. Relationship between lattice grid size d and Nyquist frequency f_{Ny} of the simulated AE signals.

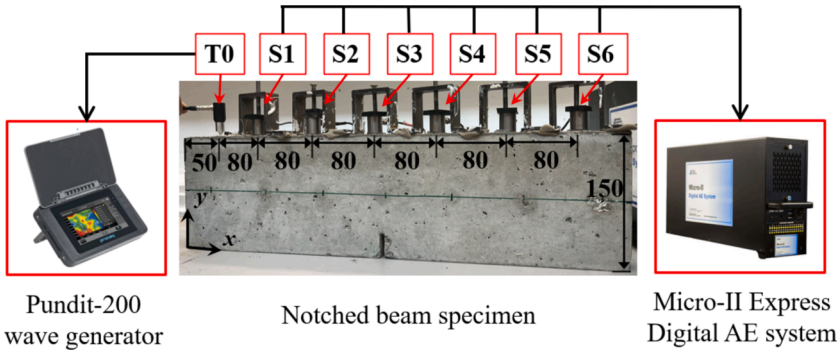

Fig. 15. Experimental setup for AE signal attenuation tests (unit: mm).

of different frequencies, including a dry-point-contact (DPC) S1803 transducer (10–160 kHz band width) [61] and a DPC S1820 transducer (150–400 kHz band width) [62]. The receivers are installed on the top surface of the specimen with a spacing of 80 mm and are connected to a AE acquisition system (Micro-II Express Digital AE [63]). Steel holders and silicone grease coupling agent are used for AE sensor installation to assure tight coupling between sensor and specimen. The positions of the DPC transducer and the six AE sensors on the specimen are consistent with those of the fracture source element and virtual AE sensors in the lattice model shown in Fig. 10.

To calibrate suitable Rayleigh damping coefficients that cover the operating frequency range of used R15α AE sensors (50–400 kHz), wave attenuation characteristics of lower- and upper-bound frequencies (namely 50 and 400 kHz) are tested. Specifically, squared waves of two different central frequency, namely 50 kHz and 400 kHz, were generated by the wave generator. The signals are received by the AE sensors and recorded by the AE acquisition system.

According to the simulation case 4 in Section 3.2 (Fig. 9), the AE signals received in experiments are dominated by R-waves. Its wave velocity $V_R(\omega)$ and material damping factor $\eta_R(\omega)$ are used to calculate the Rayleigh damping coefficients α and β in Eq. (16)-(17). The values of $V_R(\omega)$ and $\eta_R(\omega)$ are evaluated based on the received AE signals. The evaluation procedure is given in the following.

A typical AE signal with 50 kHz central frequency received by AE sensor S1 is given in Fig. 16. Two parameters can be directly obtained from the received AE signals, including the first arrival time and signal peak amplitude. The first arrival time of the signal corresponding to P-wave components is picked using the Akaike information criterion (AIC) method [64]. The P-wave velocity $V_p(\omega)$ is then estimated by a linear regression between the picked first arrival time and the distances from AE sensor to source (Eq. (7)). To reduce the picking error of AE signal peak amplitude, the amplitudes of the original signals are transformed into effective amplitudes using the average energy concept [65]. The effective amplitude at time t_i, denoted as $A_{t_i}^{(effective)}(\omega)$, is calculated as the average squared root energy of the original amplitudes $A_{t_j}(\omega)$ in the time interval $t_j \in [t_i - \frac{\Delta t}{2}, t_i + \frac{\Delta t}{2}]$ [65]:

$$A_{t_i}^{(effective)}(\omega) = \sqrt{\frac{\sum_{t_j=t_i-\frac{\Delta t}{2}}^{t_j=t_i+\frac{\Delta t}{2}} \left[A_{t_j}(\omega)\right]^2}{f_s \Delta t}} \tag{28}$$

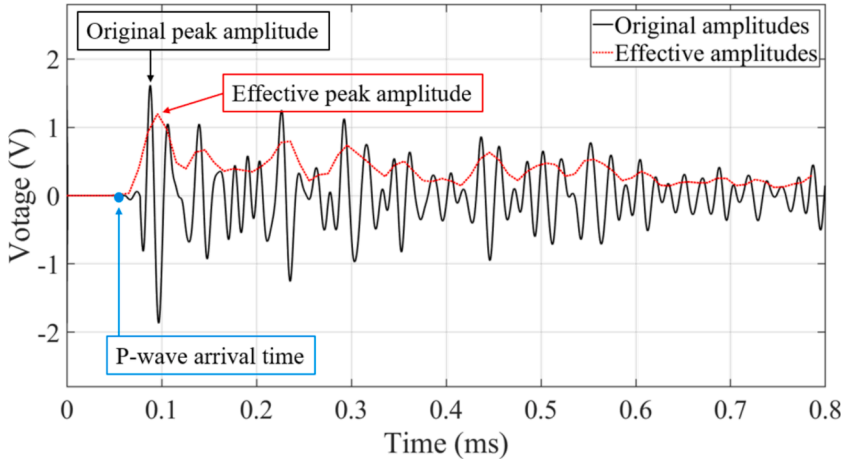

Fig. 16. A typical 50-kHz AE signal received by AE sensor S1.

where f_s is the sampling rate. Δt is the length of predefined time interval, which is selected as twice the wave period in this study [65]. The effective peak amplitude of an AE signal received by an AE sensor S_k ($k = 1\ 6$), denoted as $A_k^{(effective)}(\omega)$, is then picked as the maximum amplitude.

Wave velocity $V_R(\omega)$ and material damping factor $\eta_R(\omega)$ of dominating R-waves are then indirectly evaluated using the experimentally obtained P-wave velocity $V_p(\omega)$ and the effective peak amplitudes $A_k^{(effective)}(\omega)$. Since the Rayleigh wave velocity $V_R(\omega)$ cannot be accurately determined from experiments, it is estimated by Eq. (29)–(30) [53] based on the measured $V_p(\omega)$. The $V_R(\omega)$ are estimated as: $V_R(\omega_1) = 2285\,\mathrm{m/s}$ for $\omega_1 = 2\pi \times 50\mathrm{kHz}$ and $V_R(\omega_2) = 2349\,\mathrm{m/s}$ for $\omega_2 = 2\pi \times 400\mathrm{kHz}$.

$$V_s = V_p\sqrt{\frac{1-2\upsilon}{2(1-\upsilon)}} \tag{29}$$

$$V_R = \frac{0.87+1.12\upsilon}{1+\upsilon}V_s \tag{30}$$

The frequency-dependent material damping factor of Rayleigh waves $\eta_R(\omega)$ is calibrated using Eq. (5). Specifically, by selecting AE sensor S1 as a reference, the relative drop of peak amplitude due to material damping received by an AE sensor S_k ($k = 1\ 6$), denoted as $\widetilde{\gamma}_k(\omega)$, is normalized in Nepers (Np) as:

$$\widetilde{\gamma}_k(\omega) = \ln\left[\frac{A_1^{(effective)}(\omega)}{A_k^{(effective)}(\omega)}\right] - 0.5ln\frac{r_k}{r_1} \tag{31}$$

In Fig. 17, the total peak amplitude drop measured in experiments (first term in Eq. (31)) and theoretical values of the peak amplitude drop due to geometric spreading losses (second term in Eq. (31)) are plot in cross and triangle markers, respectively. The values of $\widetilde{\gamma}_k(\omega)$ as their differences are marked as circle symbols in Fig. 17. The value of $\eta_R(\omega)$ is then estimated by finding the best fitted line between the $\widetilde{\gamma}_k(\omega)$ values and the distances from sensor S_k to reference S_1, $\Delta r_k = r_k - r_1$. The $\eta_R(\omega)$ values are estimated as: $\eta_R(\omega_1) = 1.05\mathrm{Np/m}$ for $\omega_1 = 2\pi \times 50\mathrm{kHz}$ and $\eta_R(\omega_2) = 4.03\mathrm{Np/m}$ for $\omega_2 = 2\pi \times 400\mathrm{kHz}$. Substituting the estimated values of $V_R(\omega_1)$, $V_R(\omega_2)$, $\eta_R(\omega_1)$ and $\eta_R(\omega_2)$ into Eq. (16)–(17), the Rayleigh damping coefficients covering a interested frequency range of ($\omega_1 = 2\pi \times 50\mathrm{kHz}$, $\omega_2 = 2\pi \times 400\mathrm{kHz}$) are calculated as: $\alpha(\omega_1, \omega_2) = 4574.1\mathrm{rad/s}$ and $\beta(\omega_1, \omega_2) = 2.28 \times 10^{-9}\,\mathrm{s/rad}$.

A simulation is performed adopting the Rayleigh damping coefficients obtained from the calibration process described above. The configurations of the model are similar to that of Case 5 (see Fig. 10). The only difference is that a notch of 5-mm width and 30-mm depth is created at mid-length in the numerical model to be consistent with the physical notched beam specimen. Fig. 18a shows typical simulated AE signals received at virtual sensor S1 to demonstrate the effectiveness of proposed method in modelling the temporal attenuation of AE waves. In frequency domain, the energy of the wave is mostly located in the frequency range of 37–446 kHz that is close to the targeted frequency range of 50–400 kHz. The effectiveness of the proposed method in modelling the spatial attenuation of AE waveforms is further examined by examining the attenuation of narrow banded wave components at 50 and 400 kHz respectively. The two wave components with 50 and 400 kHz as their central frequencies are extracted using the second-order Butterworth bandpass filter [66] with a 10-kHz bandwidth, as shown in Fig. 18b. The peak amplitudes of these two extracted waves are marked in dashed line in Fig. 17a and 17b. With the damping coefficients calibrated from experiments, the spatial attenuation of simulated AE signal turns out to be comparable to experimental results.

6. Discussion

Currently, modelling the complete AE waveforms induced in concrete fracturing process is a pending problem. This complexity arises from the intricate coupling between the local discontinuity of material fracturing and the global continuity of elastic wave

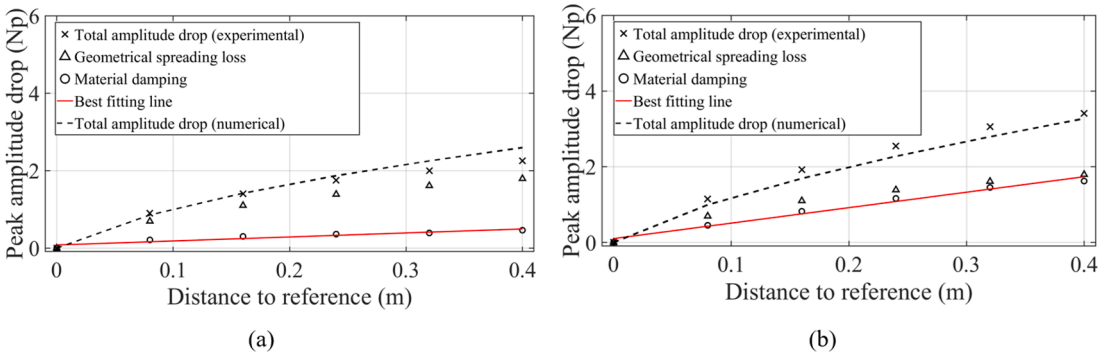

Fig. 17. Normalized amplitude drops versus sensor distances to reference S1: (a) 50 kHz central frequency AE signals and (b) 400 kHz central frequency AE signals.

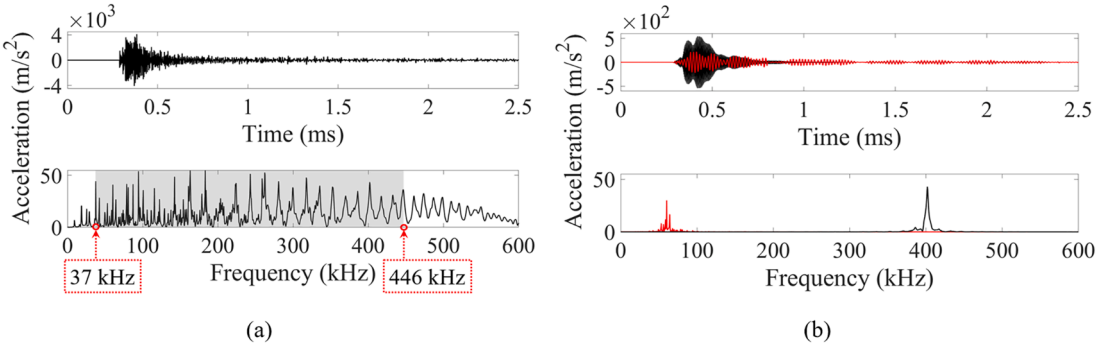

Fig. 18. Simulated AE signals received at virtual sensor S1 with calibrated Raleigh damping coefficients: (a) original signals and (b) filtered signals (50-kHz and 400-kHz central frequency components are marked in red and black lines, respectively). (For interpretation of the references to colour in this figure legend, the reader is referred to the web version of this article.)

propagation in solids. Continuum theory-based models like FEM simulate the effect of microscopic fracture over a smeared material volume and thus inherently cannot consider the dynamics of microscopic crack nucleation and growth (AE sources), although they are suitable for solving linear wave propagation problems in elastic and viscoelastic solids. The DEM models including lattice models can explicitly consider the dynamics of microscopic crack nucleation and growth though bond breakage between discrete elements; nevertheless, to date, they cannot accurately simulate the elastodynamic response of wave propagation induced by the bond breakage. This study provides general solutions to the difficulties in simulating wave propagation with attenuation using DEM models in general including lattice models, offering modelling guidelines to achieve full-waveform simulations of fracture-induced AE signals in different brittle and quasi-brittle materials. In the following, we discuss the numerical representation choices of an AE signal and the limitation of current study.

6.1. *Numerical representation of acoustic emission signals: displacement, velocity or acceleration?*

There is no consensus in literature on how to represent an AE signal in numerical modelling. Nodal displacement [67], velocity [12] and acceleration [24] were all used to numerically represent an AE signal in literature. Fig. 19 shows the displacements, velocities and accelerations of virtual AE sensor S1 in simulation case 5 adopting a 1-mm grid size d (see Fig. 10). It can be observed that the nodal acceleration of the same signal contains more high-frequency components than the nodal velocity response, and the displacement response has the least. A similar phenomenon was observed in literature that high-frequency vibration signals cannot be obtained when using displacement or velocity to represent a fracture-induced AE signal [24,25]. Different explanations were proposed for this phenomenon, e.g., attributing to the low fracture velocity of the adopted model [12] or the large numerical damping values used in the simulation [25]. A more reasonable explanation is given in the following. Consider a dynamic displacement $u(t)$ defined as a simple sine function of time t:

$$u(t) = A\sin(\omega t + \varphi) \tag{32}$$

where A, ω and φ are the amplitude, angular frequency and initial phase angle. The velocity $\dot{u}(t)$ and acceleration $\ddot{u}(t)$ are expressed as:

$$\dot{u}(t) = A\omega\sin(\omega t + \varphi + \frac{\pi}{2}) \tag{33}$$

$$\ddot{u}(t) = A\omega^2\sin(\omega t + \varphi + \pi) \tag{34}$$

As can be seen in Eq. (32)–(34), when the frequency of the signal increases, the amplitudes of the velocity and acceleration are proportional to ω and ω^2 times of those of the displacement, respectively. In an AE signal with multiple frequency components, it means that an acceleration signal is more sensitive to the higher frequency components than a displacement signal. Moreover, AE sensors, whether wideband- or resonant-type, are made from piezoelectric ceramic or crystal which charges electrically in response to applied mechanical force (stress) [54]. Physically, the electrical signals measured by an AE sensor are directly linked to the surface acceleration. It is, therefore, a logical choice to use acceleration to represent AE signals in numerical simulations.

6.2. *Limitations of current study and recommendations for future study*

The model developed in this study is based on a 2D truss-based square lattice network. This lattice network has inherent Poisson's ratios varying from 0.26 to 0.42 depending on loading directions, resulting in unequal velocities of elastic waves in different propagation directions (Fig. 9). Many alternative lattice configurations have been proposed to address the constraints associated with Poisson's ratio, by using additional shear springs [68], beam elements [69], spring birth [70], Kirkwood–Keating springs [71] and the artificial force concepts [72]. As shown by Gerstle [73], it is feasible to achieve an arbitrary Poisson's ratios using a hexagonal mesh.

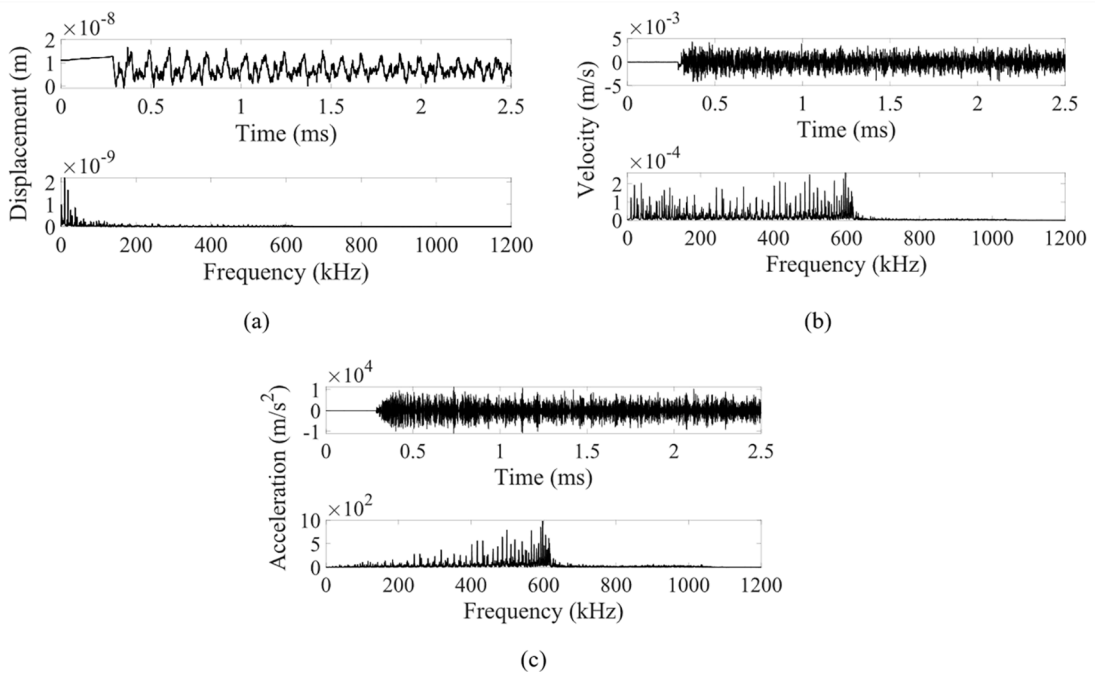

Fig. 19. Different representation choices for AE signals: (a) displacements, (b) velocities and (c) accelerations of virtual AE sensor S1 in simulation Case 5.

An example of wave propagation simulation using hexagonal lattice mesh can be found in [74]. In a future study, these advanced lattice networks can be adopted to better simulate the propagation of fracture-induced AE waves in the fracture process of concrete.

Additionally, this study adopts a 2D version of lattice model that cannot well simulate the wave propagation in real 3D concrete structures. In a future study, the proposed modelling framework can be adapted into a 3D lattice model (such as those developed in the work of Kosteski [21] and of Yue et al. [75]) to better simulate the 3D wave propagation induced by concrete fracture process. Moreover, this study only considers the AE source type of concrete tensile cracking. The coupling between tensile cracking and friction along existing cracking surfaces should be further investigated to simulate different AE source types involved in concrete mix-mode fracturing processes [76–78].

7. Conclusions

Developing deterministic models for quantitative acoustic emission (AE) source characterization relies upon accurately modelling the whole AE process, including the fracture sources and the induced elastic waves. Nevertheless, there is currently no available method that can simulate the complete transient waveforms of fracture-induced AE signals including their propagation. In this study, a lattice modelling approach is proposed to fill this research gap with a focus on simulating the wave propagation and attenuation. The noise signals in time integration procedure of dynamic lattice modelling are minimized by implementing a novel proportional-integral-derivative (PID) control algorithm. A Rayleigh damping-based calculation and calibration method is proposed to accurately model the AE wave attenuation. The proposed modelling framework can be of interest to different versions of lattice models (or even other discrete element methods) for a full-waveform simulation of fracture-induced AE signals in concrete and other brittle or quasi-brittle materials. The principal findings are synthesized as follows:

1. Feasibility of the lattice model for simulating elastic wave propagation is examined. The simulated pressure and shear wave velocities agree well with theoretical results. The geometric spreading loss of point-source wave can be accurately captured by the lattice model. Limitation of the adopted lattice model is that the simulated wave velocities are unequal in different propagation directions due to the variation of Poisson's ratio in the adopted two-dimensional squared lattice network.
2. Effect of the implemented proportional-integral-derivative (PID) control algorithm has been demonstrated. Without the PID control, non-vanishing noise signals of high amplitudes persistently exist even in the absence of a lattice element fracturing. The PID control algorithm effectively reduces the noise signals due to external loading bias in nodal accelerations.
3. A relationship is established between the lattice grid size and the frequency resolution of simulated AE signals: an appropriate lattice grid size should be no more than one eighth of the minimum targeted pressure wavelength to avoid signal aliasing.
4. A theoretical method and corresponding experimental calibration procedure are proposed to determine the Rayleigh damping coefficients for modelling the attenuation of AE signals due to material damping. The proposed method has been demonstrated by

an experiment; a comparison between the numerical and experimental results shows that the proposed method is able to capture the spatial and temporal attenuation of AE waveforms. The proposed method has the potential to be used in other numerical methods besides lattice model (e.g., finite element methods) for modelling the attenuation of AE signals generated by various sources besides fracture (e.g., stick-sliding friction along crack surfaces) in different materials besides concrete (e.g., rocks, composites or metals).

CRediT authorship contribution statement

Yubao Zhou: Writing – original draft, Visualization, Software, Resources, Methodology, Investigation, Funding acquisition, Formal analysis, Data curation, Conceptualization. **Beyazit Bestami Aydin:** Writing – review & editing, Supervision, Software, Methodology, Investigation, Data curation, Conceptualization. **Fengqiao Zhang:** Writing – review & editing. **Max A.N. Hendriks:** Writing – review & editing, Validation, Supervision, Resources, Project administration, Methodology, Funding acquisition, Conceptualization. **Yuguang Yang:** Writing – review & editing, Validation, Supervision, Resources, Project administration, Methodology, Investigation, Funding acquisition, Data curation, Conceptualization.

Declaration of competing interest

The authors declare that they have no known competing financial interests or personal relationships that could have appeared to influence the work reported in this paper.

Appendix

Derivative process of effective cross-sectional area of truss elements $A^*(d)$ in adopted 2D square lattice network

The effective cross-sectional area of a lattice element in the adopted two-dimensional truss-based lattice model, $A^*(d)$, acts as a bridge that links the elastic properties of discrete lattice elements to those of represented continuum. $A^*(d)$ is a function of the lattice grid size d and is expressed as:

$$A^*(d) = \frac{3}{2(1+\sqrt{2})} dw \tag{A.1}$$

where w is the specimen thickness. The close-form derivative process of Eq. (A.1) is given in the following. Consider a 2D isotropic continuum subjected to equally uniformed biaxial strain fields as:

$$\varepsilon_x = \varepsilon_y = \varepsilon \tag{A.2}$$

where ε_x and ε_y are strains in x and y directions, respectively. ε is a strain value. According to the Hook's law, the strains are further expressed as:

$$\varepsilon_x = \varepsilon_y = \varepsilon = \sigma\left(\frac{1-\nu}{E}\right) \tag{A.3}$$

where σ represents stress. ν and E are the Poisson's ratio and Young's modulus, respectively. The elastic strain energy stored in the considered continuum, denoted as W, is then derived as:

$$W = \frac{1}{2}\int \left(\sigma_x\varepsilon_x + \sigma_y\varepsilon_y\right)\mathrm{d}\phi = \int \sigma\varepsilon \mathrm{d}\phi = \sigma\varepsilon wA = \varepsilon^2\left(\frac{E}{1-\nu}\right)wA \tag{A.4}$$

where σ_x and σ_y are stresses in x and y directions, respectively. ϕ and A represents the volume and area of the considered 2D continuum, with $\phi = wA$. We then use the 2D square truss lattice network to discretize the considered 2D continuum (see Fig. 1). Assuming all elements (orthogonal and diagonal elements with different lengths) involved in each lattice grid size level d have same effective cross-sectional area $A^*(d)$, the total strain energy stored in the equivalent lattice representation, denoted as W^*, is then calculated as:

$$W^* = \frac{1}{2}\sum_{i=1}^{n}\frac{(F_i^e)^2 l_i}{EA^*(d)} = \frac{EA^*(d)\varepsilon^2}{2}\sum_{i=1}^{n} l_i \tag{A.5}$$

where F_i^e and L_i are the axial force and length of i-th lattice element. The total strain energy stored in the considered 2D continuum must equal that in the corresponding discrete lattice elements as:

$$W = \varepsilon^2\left(\frac{E}{1-\nu}\right)wA = W^* = \frac{EA^*(d)\varepsilon^2}{2}\sum_{i=1}^{n} l_i \tag{A.6}$$

The effective cross-sectional area $A^*(d)$ is then derived as:

$$A^*(d) = \frac{2wA}{(1-\nu)\sum_{i=1}^{n} l_i} \tag{A.7}$$

Selecting a basic unit area of area $A = d^2$ in the adopted 2D square truss lattice network (see Fig. 1) for analyses, a total of eight elements of half element length (namely $n = 8$) are involved in the basic unit area consisted of four orthogonal elements of length $l = d/2$ and four diagonal elements of length $l = \sqrt{2}d/2$. Eq. (A.7) is further expressed as:

$$A^*(d) = \frac{2wd^2}{(1-\nu)\sum_{i=1}^{8} l_i} = \frac{2wd^2}{(1-\nu)(2d+2\sqrt{2}d)} = \frac{1}{(1+\sqrt{2})(1-\nu)}wd \tag{A.8}$$

According to the work of Hrennikoff [32], the average value of inherent Poisson's ratio of the adopted square truss-based lattice model equal to 1/3. By substituting $\nu = 1/3$ into Eq. (A.8), we derive the expression of $A^*(d)$ as given in Eq. (A.1).

Data availability

Data will be made available on request.

References

[1] Scruby CB. An introduction to acoustic-emission. Journal of Physics E-Scientific Instruments 1987;20(8):947–53.
[2] Zhang FQ, et al. Probability density field of acoustic emission events: damage identification in concrete structures. Constr Build Mater 2022;327:126984.
[3] Carpinteri A, et al. Reliable onset time determination and source location of acoustic emissions in concrete structures. Cem Concr Compos 2012;34(4):529–37.
[4] Zhang F, et al. Developing a new acoustic emission source classification criterion for concrete structures based on signal parameters. Constr Build Mater 2022;318:126163.
[5] Ohno K, Ohtsu M. Crack classification in concrete based on acoustic emission. Constr Build Mater 2010;24(12):2339–46.
[6] Calabrese L, Proverbio E. A review on the applications of acoustic emission technique in the study of stress corrosion cracking. Corrosion and Materials Degradation 2020;2(1):1–30.
[7] Van Steen C, et al. Acoustic emission source characterisation of chloride-induced corrosion damage in reinforced concrete. Struct Health Monit 2022;21(3):1266–86.
[8] Zhou Y, Zhou Y, Zheng Y. AE Monitoring Corrosion-induced Deterioration of Reinforced Concrete Piles in The Simulated Marine Environment. IOP Conference Series: Earth and Environmental Science. IOP Publishing; 2019.
[9] Zheng Y, et al. Localized corrosion induced damage monitoring of large-scale RC piles using acoustic emission technique in the marine environment. Constr Build Mater 2020;243:118270.
[10] Sause MGR, Richler S. Finite element modelling of cracks as acoustic emission sources. J Nondestr Eval 2015;34(1):1–13.
[11] Minozzi M, et al. Dynamic fracture model for acoustic emission. Eur Phys J B 2003;36(2):203–7.
[12] Lisjak A, et al. Numerical simulation of acoustic emission in brittle rocks by two-dimensional finite-discrete element analysis. Geophys J Int 2013;195(1):423–43.
[13] Ji S, Di S. Discrete element modeling of acoustic emission in rock fracture. Theor Appl Mech Lett 2013;3(2):021009.
[14] Xie C, et al. Study on failure mechanism of porous concrete based on acoustic emission and discrete element method. Constr Build Mater 2020;235:117409.
[15] Cheng L, et al. Acoustic emission source location using Lamb wave propagation simulation and artificial neural network for I-shaped steel girder. Constr Build Mater 2021;273:121706.
[16] Gu XQ, et al. Discrete element modeling of shear wave propagation using bender elements in confined granular materials of different grain sizes. Comput Geotech 2020;125:103672.
[17] Schubert F, Schechinger B. Numerical modeling of acoustic emission sources and wave propagation in concrete. Journal of Nondestructive Testing(Germany) 2002;7(9):1–8.
[18] Komijani M, Gracie R, Yuan Y. Simulation of fracture propagation induced acoustic emission in porous media. Engng Fract Mech 2020;229:106950.
[19] Pan ZC, et al. A review of lattice type model in fracture mechanics: theory, applications, and perspectives. Engng Fract Mech 2018;190:382–409.
[20] Li W-J, Zhu Q-Z. An innovative quasi-bond approach to bridge continuity, anisotropic damage and macroscopic fracture of solids and structures. Int J Plast 2024;172:103829.
[21] Kosteski L, et al. The truss-like discrete element method in fracture and damage mechanics. Engng Comput 2011;28(6):765–87.
[22] Birck G, et al. Damage process in heterogeneous materials analyzed by a lattice model simulation. Engng Fail Anal 2016;70:157–76.
[23] Iturrioz I, Lacidogna G, Carpinteri A. Experimental analysis and truss-like discrete element model simulation of concrete specimens under uniaxial compression. Engng Fract Mech 2013;110:81–98.
[24] Iturrioz I, Lacidogna G, Carpinteri A. Acoustic emission detection in concrete specimens: Experimental analysis and lattice model simulations. Int J Damage Mech 2014;23(3):327–58.
[25] Minozzi M, et al. Dynamic fracture model for acoustic emission. The European Physical Journal B-Condensed Matter and Complex Systems 2003;36:203–7.
[26] Rinaldi A, et al. Lattice models of polycrystalline microstructures: a quantitative approach. Mech Mater 2008;40(1–2):17–36.
[27] Aydin BB, Tuncay K, Binici B. Overlapping lattice modeling for concrete fracture simulations using sequentially linear analysis. Struct Concr 2018;19(2):568–81.
[28] Aydin BB, Binici B, Tuncay K. Lattice simulation of concrete compressive behaviour as indirect tension failure. Mag Concr Res 2021;73(8):394–409.
[29] Aydin BB, et al. Lattice modeling and testing of aerated autoclaved concrete infilled frames. Engng Struct 2022;251:113467.
[30] Aydin BB, Tuncay K, Binici B. Simulation of reinforced concrete member response using lattice model. J Struct Engng 2019;145(9):04019091.
[31] Aydın BB, Tuncay K, Binici B. Overlapping Lattice Approach for Nonlinear Analysis of Reinforced Concrete Columns. 2018.
[32] Hrennikoff A. Solution of problems of elasticity by the framework method. 1941.
[33] Caughey T. Classical normal modes in damped linear dynamic systems. 1960.
[34] Chung J, Lee JM. A new family of explicit time integration methods for linear and non-linear structural dynamics. Int J Numer Meth Engng 1994;37(23):3961–76.
[35] Schmicker D, et al. Wave propagation analysis using high-order finite element methods: spurious oscillations excited by internal element eigenfrequencies. Technische Mechanik-European Journal of Engineering Mechanics 2014;34(2):51–71.
[36] Mirbagheri Y, et al. Reducing spurious oscillations in discontinuous wave propagation simulation using high-order finite elements. Comput Math Appl 2015;70(7):1640–58.
[37] Ziegler JG, Nichols NB. Optimum settings for automatic controllers. Trans Am Soc Mech Engng 1942;64(8):759–65.

[38] Gresil M, Giurgiutiu V. Prediction of attenuated guided waves propagation in carbon fiber composites using Rayleigh damping model. J Intell Mater Syst Struct 2015;26(16):2151–69.
[39] Zhang F. Acoustic emission-based indicators of shear failure of reinforced concrete structures without shear reinforcement. 2022.
[40] Yang Y, Cascante G, Polak MA. New method for the evaluation of material damping using the wavelet transform. J Geotech Geoenviron Engng 2011;137(8):798–808.
[41] Tian Z, et al. Modeling of the attenuation of stress waves in concrete based on the Rayleigh damping model using time-reversal and PZT transducers. Smart Mater Struct 2017;26(10):105030.
[42] Lambri O. A review on the problem of measuring non-linear damping and the obtainment of intrinsic damping. Materials Instabilities 2000:249–80.
[43] Lai N-A, Tu Z. Strauss exponent for semilinear wave equations with scattering space dependent damping. J Math Anal Appl 2020;489(2):124189.
[44] Philippidis TP, Aggelis DG. Experimental study of wave dispersion and attenuation in concrete. Ultrasonics 2005;43(7):584–95.
[45] Bormann P, Engdahl B, Kind R. Seismic wave propagation and earth models, in New manual of seismological observatory practice 2 (NMSOP2). 2012, Deutsches GeoForschungsZentrum GFZ. p. 1-105.
[46] Gaydeck P, et al. Digital deconvolution analysis of ultrasonic signals influenced by the presence of longitudinally aligned steel cables in pre-stressed concrete. Meas Sci Technol 1992;3(9):909.
[47] Meirovitch L, Methods of analytical dynamics. 2010: Courier Corporation.
[48] Ramadas C, et al. Modelling of attenuation of Lamb waves using Rayleigh damping: Numerical and experimental studies. Compos Struct 2011;93(8):2020–5.
[49] Bruna R, Riera J. Towards the simultaneous generation of the three components of the seismic acceleration on rock surface. Nucl Engng Des 1988;110(2):153–63.
[50] Iturrioz I, Riera JD. Assessment of the Lattice Discrete Element Method in the simulation of wave propagation in inhomogeneous linearly elastic geologic materials. Soil Dyn Earthq Engng 2021;151:106952.
[51] Givoli D. Non-reflecting boundary conditions. J Comput Phys 1991;94(1):1–29.
[52] Semblat JF, Lenti L, Gandomzadeh A. A simple multi-directional absorbing layer method to simulate elastic wave propagation in unbounded domains. Int J Numer Meth Engng 2011;85(12):1543–63.
[53] Morelli A, Dziewonski AM. Body wave traveltimes and a spherically symmetric P-and S-wave velocity model. Geophys J Int 1993;112(2):178–94.
[54] Matthews JR. Acoustic emission. Vol. 2. 1983: CRC Press.
[55] Desoer CA, Wang YT. On the generalized nyquist stability-criterion. IEEE Trans Autom Control 1980;25(2):187–96.
[56] Haldorsen JB. Spatial aliasing. in SEG International Exposition and Annual Meeting. 2020. OnePetro.
[57] Walraven JC. Model Code 2010-Final Draft: Volume 1. Vol. 65. 2012: fib Fédération internationale du béton.
[58] Pal P. Dynamic Poisson's ratio and modulus of elasticity of pozzolana portland cement concrete. International Journal of Engineering and Technology Innovation 2019;9(2):131–44.
[59] MISTRAS, *R15α Sensor*. 2011: Princeton Jctction, NJ 08550, USA, Products & System Division.
[60] Pundit, Pundit 200: Concrete properties analysis using ultrasound pulse velocity. 2021: Screening Eagle Technologies AG, Ringstrasse 2, 8603 Schwerzenbach - Zurich.
[61] ACS, *Ultrasonic transducer S1803*. 2023: ACS-Solutions GmbH Science Park 2 66123 Saarbrücken, Germany.
[62] ACS, *Ultrasonic transducer S1820*. 2023: ACS-Solutions GmbH Science Park 2 66123 Saarbrücken, Germany.
[63] MISTRAS, *MICRO-II – COMPACT PCI AE CHASSIS*. 2011: Princeton Jctction, NJ 08550, USA, Products & System Division.
[64] Liu MZ, et al. A new method for arrival time determination of impact signal based on HHT and AIC. Mech Syst Sig Process 2017;86:177–87.
[65] Weaver RL, Sachse W. Diffusion of ultrasound in a glass bead slurry. J Acoust Soc Am 1995;97(4):2094–102.
[66] Hussin SF, Birasamy G, Hamid Z. Design of butterworth band-pass filter. Politeknik & Kolej Komuniti Journal of Engng Technol 2016;1(1).
[67] Prosser WH, et al. Finite element and plate theory modeling of acoustic emission waveforms. J Nondestr Eval 1999;18(3):83–90.
[68] Griffiths D, Mustoe GG. Modelling of elastic continua using a grillage of structural elements based on discrete element concepts. Int J Numer Meth Engng 2001;50(7):1759–75.
[69] Karihaloo BL, Shao P, Xiao Q. Lattice modelling of the failure of particle composites. Engng Fract Mech 2003;70(17):2385–406.
[70] Parisi A, Caldarelli G. Self-affine properties of fractures in brittle materials. Physica A 2000;280(1–2):161–5.
[71] Monette L, Anderson M. Elastic and fracture properties of the two-dimensional triangular and square lattices. Model Simul Mater Sci Engng 1994;2(1):53.
[72] Baudet V, et al., New mass-spring system integrating elasticity parameters in 2D. 2007.
[73] Gerstle WH, Introduction to practical peridynamics: computational solid mechanics without stress and strain. Vol. 1. 2015: World Scientific Publishing Company.
[74] Suiker ASJ, Metrikine AV, de Borst R. Comparison of wave propagation characteristics of the Cosserat continuum model and corresponding discrete lattice models. Int J Solids Struct 2001;38(9):1563–83.
[75] Yue Q, et al. A phase-field lattice model (PFLM) for fracture problem: theory and application in composite materials. Compos Struct 2023;323:117432.
[76] Wang Q, et al. Modeling of both tensional-shear and compressive-shear fractures by a unified phase-field model. App Math Model 2023;117:162–96.
[77] Yue Q, et al. An efficient adaptive length scale insensitive phase-field model for three-dimensional fracture of solids using trilinear multi-node elements. Int J Mech Sci 2023;253:108351.
[78] Yue Q, et al. An adaptive phase-field model based on bilinear elements for tensile-compressive-shear fracture. Comput Math Appl 2022;105:112–35.